JOURNAL OF MATERIALS SCIENCE 18 (1983) 430–438

An investigation on the nature of porosity in hardened cement pastes using small angle neutron scattering

D. PEARSON, A. ALLEN*, C. G. WINDSOR*
*Materials Development Division and *Materials Physics Division, A.E.R.E. Harwell, Didcot, UK*

N. McN. ALFORD, D. D. DOUBLE
Department of Metallurgy and Science of Materials, Oxford University, Oxford, UK

The porosity and pore-size distribution in hardened cement paste have been measured by several techniques which often give conflicting results. Small angle neutron scattering is a new technique in the area of cement technology, which enables information to be obtained at the fine end of the pore distribution (less than approximately 30 nm diameter using this machine) without any specimen drying or pretreatment. The technique indicates a bi-modal distribution of spherical or near spherical pores with diameters of approximately 5 and 10 nm, accounting for less than about 2% of the total paste volume. The pores seem relatively unaffected by the water to cement ratios investigated; however, drastic effects do seem to occur on drying at 105° C.

1. Introduction

Portland cement pastes, grouts and cements are used for the immobilization of a wide variety of radioactive wastes. One property of the waste form which is of considerable interest is the rate at which radionuclides are released to an aqueous environment. A fundamental parameter influencing this leaching behaviour is the porosity of the cement monolith. At the ultra fine end of the porosity size distribution, the pores present will represent a very large surface area to volume ratio and this may have a large influence on radionuclide dissolution, which must be considered as the first step in a leaching process.

The methods currently used to obtain data on total porosity and pore-size distribution in hardened cement paste (HCP) often produce conflicting results. Total porosity may be measured by calculating the volume of a sample from its geometric dimensions and determining its weight. If the density of the sample is known, then an estimate of the void volume can be made. Porosity has also been measured by determining the non-evaporable water content of the sample [1].

The method of porosity determination used in this study was water displacement pycnometry. This method measures the weight of the specimen in water, the surface dry weight, and, finally, the oven dry weight. In this way, the apparent density, the pore volume and the porosity may be determined [2]. Pycnometry using liquids such as methanol, paraffin, or toluene instead of water, gives slightly different results believed to be due to molecular size effects [3]. Feldman [4] has used helium pycnometry to determine total pore volume, which has two advantages – the helium is non-reactive (unlike the liquids) and the measurement is relatively rapid.

Pore-size distributions may be measured by Mercury Intrusion Porosimetry (MIP) [5], a technique which appears to work well for many materials but disappointingly for HCP. Two problems in particular are that the pore-size distributions are sensitive to the pore entry diameter and also that the pore volume recorded by MIP is often much less than that recorded by other methods [6]. In the past, the "missing" porosity has been ascribed by some authors [5, 7] to the very fine

0022–2461/83/020430–09$03.58/0

end of the distribution corresponding to diameters too small to be penetrated by pressurized mercury.

The use of gas adsorption isotherms to determine the fine scale porosity has been criticized [8] in that the distribution mode is almost exclusively below 10 nm diameter. This can be grossly misleading as the true mode in the pore-size distribution is much greater [8, 12].

The present authors wished to determine the extent of porosity below the limit of MIP both from the point of view of radionuclide dissolution and to verify whether this could be the pore volume missed by the mercury. Also, using the small angle neutron scattering (SANS) technique, it is possible to generate data on pore shape. It should be noted that MIP necessarily assumes a cylindrical pore model which, for HCP, may not be correct.

2. Theory of small angle neutron scattering [9]

The technique produces neutron contrast due to differences in neutron/nucleon interactions between small, particulate regions in a general background medium. Initially, one needs to make no assumptions about the identity of the particles which, in this instance, may be cement gel; calcium hydroxide crystals; or pores (which may be either air filled or water filled). The final decision as to the identity of the scattering particle phase often becomes clear after data analysis.

The SANS of interest, with the neutron wavelength used, occurs at less than five degrees and can be divided for analysis into two regions:

(a) at low scattering angles the Guinier approximation holds [10]:

$$\sum_{\mathrm{SAS}}(\mathbf{Q}) = (\text{volume concentration}) \times (\text{contrast}) \times (V_{\mathrm{PT}}) \times \exp(-Q^2 R_{\mathrm{G}}^2/3), \quad (1)$$

where $\mathbf{Q}$ is the change in neutron wave vector on scattering, R_{G} is the radius of gyration of a scattering particle with a volume V_{PT} (the "radius of gyration" of a volume is the mean squared distance of all points within that volume, from the centroid – for a uniform sphere of radius R_{S}, $R_{\mathrm{G}}^2 = 3R_{\mathrm{S}}^2/5$) and Q is the magnitude of $\mathbf{Q}$.

(b) at larger scattering angles the Porod approximation applies:

$$\sum_{\mathrm{SAS}}(\mathbf{Q}) = (\text{volume concentration}) \times (\text{contrast}) \times \left(\frac{S_{\mathrm{PT}}}{V_{\mathrm{PT}}}\right) \times \left(\frac{2\pi}{Q^2}\right), \quad (2)$$

where S_{PT} is the surface area of the particle.

The Porod approximation is used to obtain a more reliable estimate of the surface to volume ratio by combining it with a third equation [10]:

$$\lim_{Q \to \infty} \frac{[Q^4 \Sigma_{\mathrm{SAS}}(\mathbf{Q})]}{\int_0^{\infty} Q^2 \Sigma_{\mathrm{SAS}}(\mathbf{Q})\, \mathrm{d}Q} = \frac{S_{\mathrm{PT}}}{\pi V_{\mathrm{PT}}}. \quad (3)$$

These equations are derived for a single scattering particle size but remain applicable for a size distribution whereby:

$$V_{\mathrm{PT}} \text{ becomes } \overline{V}_{\mathrm{PT}},$$

the volume weighted mean volume

$$\frac{S_{\mathrm{PT}}}{V_{\mathrm{PT}}} \text{ becomes } \left(\frac{\overline{S_{\mathrm{PT}}}}{\overline{V}_{\mathrm{PT}}}\right),$$

the volume weighted mean surface to volume ratio.

To relate R_{G} to these volume weighted means, we must deduce the scattering particle size distribution using computer analysis.

Certain particle shapes such as spheres, long cylinders, or discs, each produce specific $\Sigma_{\mathrm{SAS}}(\mathbf{Q})$ functions. Using each of these functions in turn, a program by Vonk [11] varies the particle size distribution while checking for correlation with the experimental data until an optimum particle-size distribution is obtained.

Poor correlation with the raw data often removes one or more of these specific shapes from consideration, while the rest are tested by obtaining $(\overline{S_{\mathrm{PT}}}/\overline{V}_{\mathrm{PT}})$ from Equation 3. In fact, Equation 3 is highly discriminatory between shapes used in the Vonk plot which have given plausible fits to the experimental data (correlation of a few per cent).

If log intensity is plotted against Q^2 from Equation 1, the intercept at zero $\mathbf{Q}$ gives, after normalization, the scattering at zero incident beam

TABLE I Flexural strengths* of specimens

Specimens	Strength† (MPa)	
	14 days	27 days
A type	14.6	16.7
B type	8.3	9.0

*Centre point loading.
†Average of four readings.

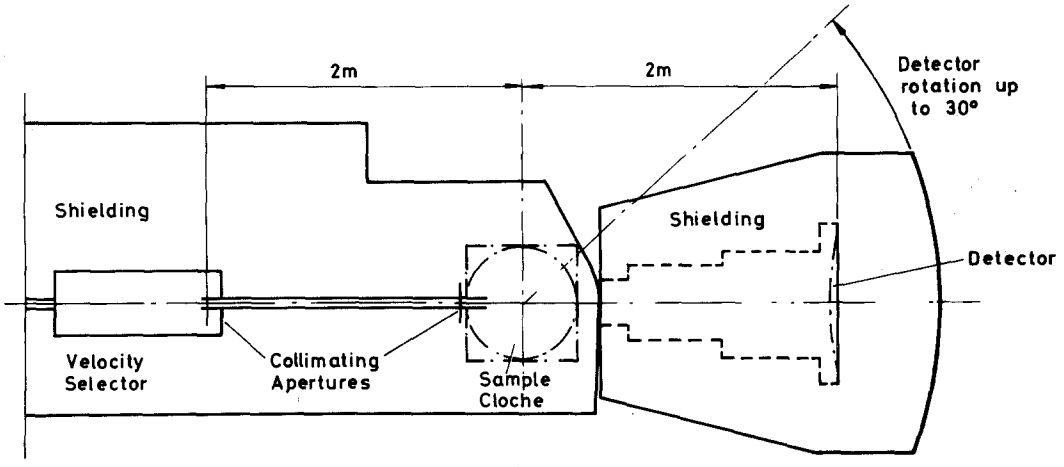

Figure 1 Plan of the Pluto small angle neutron scattering spectrometer.

deflection. From Equation 1, we see that in this case:

$$\Sigma_{SAS}(0) = (\text{vol. conc.}) \times (\text{contrast}) \times \overline{V_{PT}}. \quad (4)$$

$\overline{V_{PT}}$ is determined from the particle-size distribution and shape as deduced by the Vonk plot. The contrast for any particle phase with respect to a mean sample medium can be calculated when the atomic composition and density of the phases present are known, together with the neutron scattering length of the phases. Equation 4 can, therefore, be used to obtain the volume concentration of the given particle shape and particle distribution.

3. Experimental methods

Four sets of specimens were prepared as beams using a conventional ordinary portland cement, distilled water, a 5 min mixing time, and hand tamping.

(A) 0.2 water to cement ratio (w/c), cured in high humidity for 5 days and then stored under water for 31 days.

(B) 0.6 w/c, cured and stored as A.

(C) 0.6 w/c, cured and stored as A but after 28 days, dried to 11% r.h. for 24 h and then fully immersed in heavy water (D_2O) until neutron irradiated.

(D) 0.6 w/c, cured and stored as A but after 29 days, oven dried at 105° C for 24 h and kept dry until neutron irradiation.

Final storage was extended by up to 18 h owing to the length of irradiation, the sequence of testing the samples being B, D, C, A.

The conditions for Specimen C were chosen in order to remove pore water without significantly altering the structure. The light water was consequently replaced with heavy water which is a much stronger neutron scatterer, thus giving higher contrast levels.

Eight beams of each specimen type were

TABLE II Composition* of unhydrated cement powder

Component	wt%	Density† ($g\,cm^{-3}$)	Molecular wt	Mol/100 g dry cement
Free CaO	2.5	3.32	56.1	0.045
$3CaO \cdot SiO_2 = C_3S$	57.5	3.13	228.4	0.252
$2CaO \cdot SiO_2 = C_2S$	14.0	3.35	172.3	0.081
$3CaO \cdot Al_2O_3 = C_3A$	11.7	3.04	270.3	0.043
$4CaO \cdot Al_2O_3 \cdot Fe_2O_3 = C_4AF$	7.6	3.97	486.0	0.016
MgO	1.5		40.3	0.037
$SO_3 = \bar{S}$	2.5		80.1	0.031
Na_2O	0.4		62.0	0.006
K_2O	0.6		94.2	0.006

*Loss on ignition = 1.5%.
†Density of dry cement = 3.1 $g\,cm^{-3}$.

TABLE III Simplified hydration reactions

$$2C_3S + 5.5\,H_2O \rightarrow C_3S_2 \cdot 2.5w^* + 3Ca(OH)_2$$
$$2C_2S + 3.5\,H_2O \rightarrow C_3S_2 \cdot 2.5w + Ca(OH)_2$$
$$C_3A + Ca(OH)_2 + 12H_2O \rightarrow C_4A \cdot 13w$$
$$C_3A + CaSO_4 \cdot 2w + 10H_2O \rightarrow C_3A \cdot CaSO_4 \cdot 12w$$
$$C_4AF + 2Ca(OH)_2 + 10H_2O \rightarrow C_6AF \cdot 12w$$
$$CaO\ (\text{free lime}) + H_2O \rightarrow Ca(OH)_2$$

*w represents bound water.

TABLE V Coherent scattering lengths for slow neutrons

Element	b ($\times 10^{-14}$ m)	Element	b ($\times 10^{-14}$ m)
Ca	0.49	Na	0.35
Si	0.42	K	0.35
Al	0.35	O	0.58
Fe	0.96	H	−0.378
S	0.31	D	0.65
Mg	0.54		

prepared. Flexural strengths (centre point loading) were determined on wet specimens at 14 and 27 days, allowing a check to be made on the strength development, hydration progress, and uniformity of preparation (Table I).

Pieces of the broken specimens from the bend tests were cut to roughly 1 cm × 1 cm × 0.4 cm slices with a water-flooded diamond saw. These were then ground on wet carbide papers to a thickness of less than 1 mm (which allowed insertion into the SANS specimen holder). They were then replaced in water.

Some larger pieces were also cut from the broken pieces and used either immediately or subsequently for water pycnometry or MIP. Experimental details of these techniques are described elsewhere [2, 12].

Fig. 1 shows the layout of the Pluto SANS spectrometer [13]. The specimen is placed in a small glass cell and irradiated for about 6 h. The detectors feed to a PDP-11 computer which collects and radially averages the data before transfer to a hub computer for background subtraction and normalization [14], followed by Guinier and Porod plotting. The size-distribution analysis is performed on an IBM 3033 main frame computer.

4. SANS contrast in HCP

Table II gives an analysis of the dry cement powder used, along with the standard cement notation. Table III gives simplified hydration reactions once water is available. Table IV combines Tables II and III to give an estimated fully hydrated composition when all the anhydrous material has been used up.

The coherent scattering lengths for neutrons by the various elements found in cement are shown in Table V [9]. Tables II and IV (when converted to volume concentrations) combined with Table V produce the coherent scattering length density of the various phases with bound water (H_2O or D_2O) contents corresponding to zero and complete hydration – Tables VI and VII (coherent scattering length density, ρ, is the product of the mean scattering length per atom and the atomic number density).

The scattering length densities for intermediate degrees of hydration have been linearly interpolated between the extremes in Tables VI and VII. The datum points used for the interpolation are

zero hydration: 0% bound water
3.1 g cm^{-3} density
fully hydrated: 22.4% bound water by weight
2.20 g cm^{-3} density.

Table VIII gives the density and porosity values

TABLE IV Composition of fully hydrated* cement pastes

Component	wt%	Density‡ (g cm^{-3})	Molecular wt	Estimated moles produced from 100 g dry cement
$C_3S_2 \cdot 2.5w$†	43.8	2.15	333.5	0.167
$C_4A \cdot 13w$	5.3	2.02	560.4	0.012
$C_3A \cdot CaSO_4 \cdot 12w$	15.2	1.99	622.5	0.031
$C_6AF \cdot 12w$	10.2	2.90§	814.2	0.016
$Ca(OH)_2$	22.7	2.23	74.1	0.389
$Mg(OH)_2$	1.7	2.40	58.3	0.037
NaOH	0.4	2.13	30.0	0.012
KOH	0.5	2.04	48.1	0.012

*Bound water content is 22.4% by weight.
†w represents bound water.
‡Density of fully hydrated paste is about 2.2 g cm^{-3}.
§Estimate.

TABLE VI Volume concentration and scattering length density of major phases present in unhydrated cement powder

Phase	Volume conc. (%)	Scattering length density $\rho_b \times 10^{14}$ (m^{-2})
CaO	2.3	3.80
C_3S	56.9	3.94
C_2S	13.0	4.34
C_3A	11.9	3.81
C_4AF	5.9	5.09
mean		3.94* × 10^{14} m^{-2}
H_2O†	–	−0.60
D_2O†	–	6.28

*Only the phases stated have been used to derive the mean, accounting for a total volume concentration of 90%.
†Any water present in the reacted cement will be a saturated solution of calcium hydroxide (approx. 1 g CaO/litre) but this has little effect on the scattering length density given for the water.

of the pastes from the water pycnometry. The degree of hydration can be calculated by assuming that the apparent density is the weight of the paste and pores in 1 cm^3, the porosity fraction is then subtracted and the turee paste density calculated. The bound water content is obtained by linear interpolation and indicates the soundness of the technique by producing realistic values as shown in Table VIII.

The SANS contrast is now simply obtained as $|\rho_{\text{particle}} - \rho_{\text{average medium}}|^2$ (it does not matter if ρ_{particle} is greater or less than ρ_{medium}) and is given in Table IX.

5. Results and discussion

From measurements of the SANS cross-section (Σ_{SANS}), the volume weighted mean scattering volume ($\overline{V}_{\text{PT}}$), and the contrast values deduced from the previous section, it has been possible to estimate the required concentrations of various scattering phases to give the SANS observed. By comparing results from all of the samples, the identity of the scattering phase giving rise to the SANS has been established as being porosity.

Fig. 2 shows the MIP traces of Specimens A and B at 36 days after manufacture for comparison with the SANS results. The MIP traces are significantly different from each other, in particular, there is, as expected, a large difference in the volume intruded.

5.1. General points

Guinier plots of Cements A, B and C have prominent linear regions which indicate a well-developed small particle-size distribution and, in fact, corresponds to $R_G = 2$ to 2.5 nm, as well as a larger particle-size distribution at $R_G = 5$ nm. These prominent regions disappear in cement *D* leaving a continuous distribution.

5.2. Volume concentration and nature of the pores

Table X gives the required volume concentration of the named particle phases at the size distribution predicted by the Vonk plot which would produce the experimentally observed SANS. We must consider that the particles giving rise to the scattering could be either gel, calcium hydroxide crystals, water-filled pores, or air-filled pores.

Air-filled pores of the correct size range determined by the Vonk plot could account for the scattering in Pastes A and B. If the pores were air-

TABLE VII Volume concentration and scattering length density of major phases present in fully reacted cement paste

Phase	Volume concentration (%)	Scattering length density $\rho_b \times 10^{14}$ (m^{-2})	
		Hydrated	Deuterated
$C_3S_2 \cdot 2.5w$*	44.8	2.29	4.28
$C_4A \cdot 13w$	5.8	0.91	6.47
$C_3A \cdot CaSO_4 \cdot 12w$	16.8	1.27	6.03
$C_6AF \cdot 12w$	7.8	2.22	7.50
$Ca(OH)_2$	22.3	1.61	5.33
$Mg(OH)_2$	1.6	2.32	7.39
KOH	0.6	1.20	3.45
NaOH	0.4	1.76	5.06
mean†		1.87 × 10^{14} m^{-2}	5.29 × 10^{14} m^{-2}

*w represents H_2O in the hydrated paste and D_2O in the deuterated paste.
†As in Table VI, only the phases named have been used to derive the mean. The sum of these phases is not 100%.

TABLE VIII Bound water content calculated from density and porosity

	Specimen A		Specimens B, C, D	
	14 day	34 day	14 day	34 day
Apparent density (g cm^{-3})	2.08	2.24	1.42	1.56
Porosity (%)	23	19	46	41
Paste density (g cm^{-3})	2.71	2.76	2.65	2.64
Bound water content (wt%)	9.7	8.5	11.2	11.5

filled, however, the D_2O exchange treatment of C would probably still leave air-filled pores and no significant change in scattering should therefore be seen between A, B and C. Intuitively, as water seems to have exceptionally easy access to the free space in cement, it seems reasonable that the pores would be water filled rather than air filled. We therefore discount this hypothesis.

It is immediately seen from Table X that hydroxides (and deuteroxides), as well as the different forms of gel considered, could not account for the decline in SANS which occurs in Specimen C compared with both A and B.

Water-filled pores give a much more realistic explanation as to the nature of the scattering "particles". We assume that the water-filled pores are surrounded by hydrated gel. At the one extreme, the gel has hydrated to hold the average bound water content (obtained from the linear interpolation procedure as approximately 9.2% for A and 11.4% for B, C and D). At the other extreme, the gel has hydrated fully (bound water content 22.4%). Using these values to obtain the contrast and replacing in Equation 4, we find that for Specimen A, the volume concentration of water-filled pores is 0.5 (9.2% bound water) to 1.1 (22.4% bound water). For Specimen B these values are 0.7 and 1.3, respectively.

These pores should have approximately the same volume concentration in Specimen C, and we see that this is indeed the case if we assume that the light water in the pores is replaced by heavy water and that the hydrated gel becomes deuterated by molecular exchange. This gives a volume concentration of 0.6 (11.4% bound water) to 1.6 (22.4% bound water). Specimen D is in agreement with these results if we assume that the pores, after drying, become air filled while the level of bound water in the gel does not significantly decline. This would give a volume concentration of 0.5 (11.4% bound water) to 1.0 (22.4% bound water).

We postulate, therefore, that the particles are pores. The SANS is due to H_2O-filled pores in A and B, D_2O-filled pores in C, and air-filled pores in D. In C, the paste surrounding the pores is assumed to be fully deuterated. Whether the level of hydration (or deuteration) in the paste surrounding the pores is total or merely a characteristic value dependent on the mode of cement preparation, is not absolutely determined.

TABLE IX Contrasts of phases against the average medium: $(\rho_{bp} - \rho_{bo})^2$

Phase	Contrast × 10^{28} (m^{-4})		
	Unhydrated cement powder	Hydrated paste	Deuterated paste
Air-filled pores	15	3.7	28
H_2O-filled pores	20	6.4	34
D_2O-filled pores	5.5	19	1
Hydroxides	5	0.1	13
Deuteroxides*	2	12	negligible
$Mg(OD)_2$	12	30	4.5
Hydrated gel	2.7	2†	8.6†
Deuterated gel	0.1	5.5†	10†

*Excluding $Mg(OD)_2$.

†For the gels which are in their own paste, e.g. hydrated gels in hydrated paste, the maximum contrasts to be expected are given: for gels not in their own paste, e.g. hydrated gels in deuterated paste, the contrast of the most likely phase (e.g. $C_3S_2 \cdot 2.5w$ for hydrated gels) is given.

5.3. Shape

When the Vonk program is used for disc-shaped pores, the fit to the experimental data for the best-fit size distribution is bad (several times worse correlation than for other shapes). Long, cylindrical pores with lengths of tens of nanometres and diameters approximately 3 nm give reasonable correlation to the original data. However, these cylindrical pores would be such effective scatterers as to require a negligibly small volume concentration in order to produce the observed scattering. Unfortunately, the Vonk program cannot investigate a needle-shaped model with infinitestimal cross-section, these would, however, be such poor scatterers as to require ridiculously large volume concentrations to account for the SANS observed. The spherical pore model gives a better fit than that for cylinders, and also an intermediate volume concentration between cylinders and needles, it has therefore been assumed in deriving the other results.

It is true that the pores may not be exactly spherical, but, if they have a cylindrical component, the diameters and lengths will give good approximations to the true volumes.

Although counting times were generally insufficient to obtain good Porod data, rough estimates of the Porod region were used to obtain surface to volume ratio data from Equation 3. These data are necessarily a volume weighted mean over the whole pore-size distribution, but the prominence of the small peak in the distribution and the surface to volume value obtained, does suggest a pore shape which (even if non-spherical) is of low eccentricity.

5.4. Size

Fig. 3 shows the volume weighted pore-size distribution for each specimen using Vonk's program and assuming sphericity, it shows several significant features:

(i) Specimens A, B, C and D all show a peak in the distribution at a diameter of about 5 nm and Specimens A, B and C show a smaller peak at around 10 nm while Specimen D shows a continuous distribution;

(ii) drying Specimen D at 105° C seems to have a drastic effect on the pore structure. This suggests that pretreatment of specimens before using other techniques to measure porosity, such as MIP or helium pycnometry, significantly alters the pore distribution at the fine end (even the drying at 11% r.h. in Specimen C seems to have affected the structure). This might indicate some collapse and fragmentation of the surrounding structure;

(iii) despite a relatively large difference in w/c (in terms of technologically useful mixes) between Specimens A and B, there is very little difference in the pore-size distribution found at the small end by SANS. The difference in w/c is clearly having large effects on the paste as the strength results in Table I and the MIP data in Fig. 2 show. If we assume that the pores are between the cement gel, then it appears that the morphology of the pores (and therefore the gel surrounding them) is unchanged by the water to cement ratio. The electron micrograph in Fig. 4 [17] reinforces this view, seeming to show pore spaces in between the gel particles which are of a similar size to those pores found by SANS. This may indicate that strength is determined by flaws at a macro level, a conclusion which has beeen recently reached by authors using unrelated techniques [15, 16];

(iv) the peak in the distribution at a diameter of about 10 nm agrees fairly closely with that seen in the mercury porosimeter. Unfortunately, the porosimeter used is incapable of giving penetration at sizes as low as 5 nm so that further correlation between the two techniques is impossible;

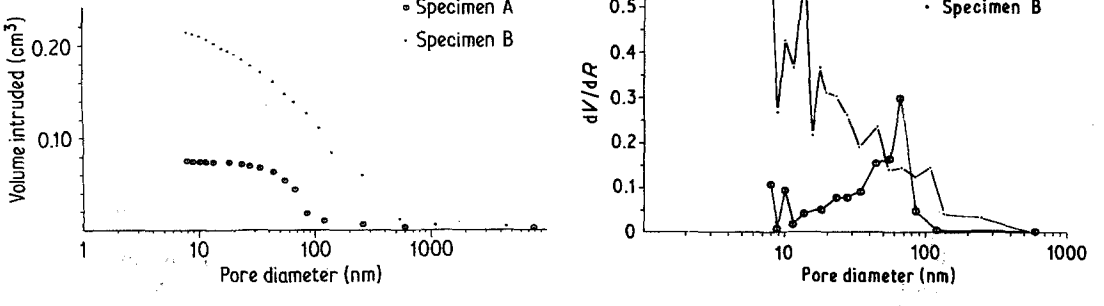

Figure 2 Mercury intrusion porosimetry results for Specimens A and B at 36 days.

TABLE X Required volume concentrations of named phases occurring as small particles which would alone give rise to the SANS observed

Phase	Volume concentration (%)				
	Specimen A	Specimen B	Specimen C*		Specimen D
			Hydrated	Deuterated	
Air-filled pores	0.7	1.0	0.2	0.07	0.8
H_2O-filled pores†	0.7 1.1	0.7 1.3	0.13	0.06	0.5 1.0
D_2O-filled pores‡	–	–	0.14	0.6 1.6	–
Hydroxides	3.1	5.0	1.0	0.2	4.0
Deuteroxides	–	–	0.27	3.3	–
$Mg(OD)_2$	–	–	0.08	0.2	–
Hydrated gels	4.0	4.5	0.8	0.2	1.5
Deuterated gels	–	–	0.3	0.2	3.2

*Considers surrounding medium as being C–S–H (hydrated) gel or C–S–D (deuterated) gel at the characteristic degree of hydration of the specimen.
†Second figure indicates volume concentration of H_2O-filled pores occurring if gel in surrounding medium is fully hydrated.
‡Second figure indicates volume concentration of D_2O-filled pores occurring if gel in surrounding medium is fully deuterated.

(v) there seems to be fairly good correlation between SANS and capilliary condensation in some instances [8]. SANS indicates a bimodal distribution of pore sizes which is corroborated in some condensation results. The disappearance of the 10 nm peak in some capilliary condensation data may be due to drying techniques before testing which, as SANS shows, can have quite significant effects.

6. Conclusions

(1) No single technique appears to fully describe the pore structure in HCP accurately.

(2) Preparation of samples for examination can significantly alter structures at sizes below about 30 nm diameter.

(3) There is, at an upper limit, 2% of porosity with diameters below about 30 nm.

(4) Water to cement ratio seems to have negligible effect on the volume or size distribution of these fine pores and hence, we assume, the gel.

(5) The pores investigated are probably of very low eccentricity or even spherical.

(6) There is a bimodal distribution of pores in HCP at diameters of approximately 5 and 10 nm.

Acknowledgements

This work has been commissioned by the Depart-

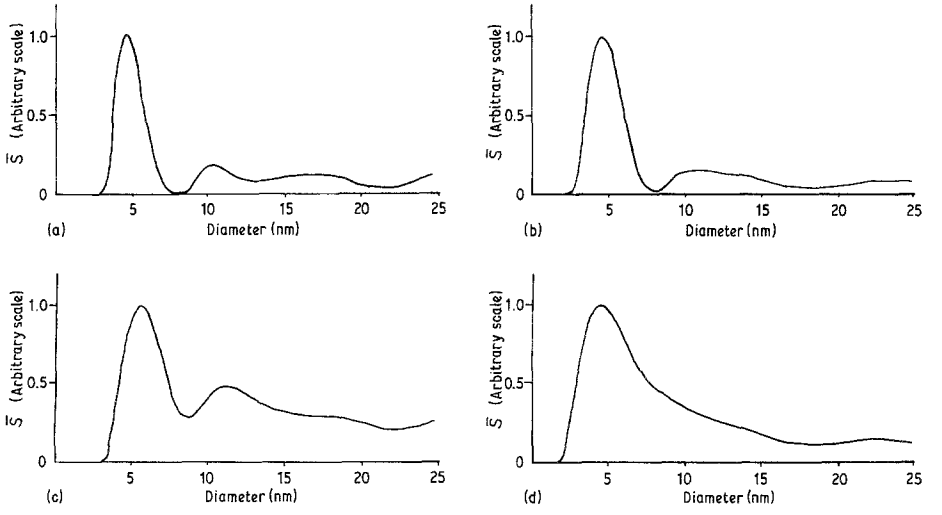

Figure 3 Volume weighted pore-size distribution for each specimen.

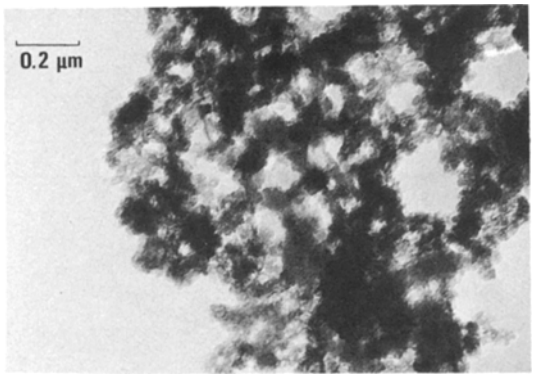

Figure 4 Wet cell transmission electron micrograph showing gel particles.

ment of the Environment as part of its radioactive waste research programme. The results will be used in the formulation of Government policy but at this stage do not necessarily represent Government policy.

References

1. D. M. ROY and G. R. GOUDA, *Cem. Conc. Res.* **3** (1973) 807.
2. N. McN. ALFORD, *ibid.* **10** (1980) 263.
3. T. C. POWERS and T. L. BROWNYARD, *Bull. Portland Cement Assoc.* **22** (1948) 692.
4. R. F. FELDMAN, *Cement Technol.* **3** (1972) 5.
5. D. N. WINSLOW and S. DIAMOND, *J. Mater. Sci.* **5** (1970) 564.
6. N. McN. ALFORD and D. D. DOUBLE, in "Proceedings of the International Symposium on Adsorption at the Gas–Solid and Liquid–Solid Interface", (Elsevier Scientific Publishing Co., Oxford, Amsterdam and New York, 1981) p. 259.
7. J. J. BEAUDOIN, *Cem. Conc. Res.* **9** (1979) 771.
8. S. DIAMOND, *ibid.* **1** (1971) 531.
9. G. E. BACON, "Neutron Diffraction", 2nd edn (Oxford University Press, Oxford, London and New York, 1962).
10. A. GUINIER and G. FOURNET, "Small Angle Scattering of X-Rays", (Riley, New York, 1955).
11. C. G. VONK, *J. Appl. Cryst.* **9** (1976) 433.
12. N. McN. ALFORD and A. RAHMAN, *J. Mater. Sci.* **16** (1981) 3105.
13. A. H. BASTON and D. H. C. HARRIS, "Neutron Beam Instruments at Harwell", A.E.R.E. Report No. R9278 (1978).
14. A. ALLEN, C. G. WINDSOR and D. PEARSON, *J. Phys. (D) Appl. Phys.* **15** (1982) 1817.
15. J. D. BIRCHALL, A. J. HOWARD and K. KENDALL, *Nature* **289** (1981) 388.
16. N. McN. ALFORD, *Cem. Conc. Res.* **11** (1981) 605.
17. D. D. DOUBLE, N. L. THOMAS and D. A. JAMESON, in "Proceedings of the 7th International Congress on the Chemistry of Cement" Vol. II (Editions Septima, Paris, 1980) p. 256.

Received 23 June
and accepted 12 July 1982